






Open Archive Toulouse Archive Ouverte (OATAO)

OATAO is an open access repository that collects the work of Toulouse researchers and makes it freely available over the web where possible

This is an author's version published in: <http://oatao.univ-toulouse.fr/23530>

Official URL: <https://doi.org/10.1016/j.solmat.2015.06.009>

To cite this version:

Chane-Ching, Jean-Yves  and Foncrose, Vincent  and Zaberca, Oana  and Lagarde, Delphine and Balocchi, Andréa and Marie, Xavier and Blon, Thomas and Puech, Pascal and Bodeux, Romain *A gas-templating strategy to synthesize CZTS nanocrystals for environment-friendly solar inks.* (2015) *Solar Energy Materials and Solar Cells*, 141. 364-371. ISSN 0927-0248

Any correspondence concerning this service should be sent to the repository administrator: tech-oatao@listes-diff.inp-toulouse.fr

A gas-templating strategy to synthesize CZTS nanocrystals for environment-friendly solar inks

Jean-Yves Chane-Ching^{a,*}, Vincent Foncrose^a, Oana Zaberca^a, Delphine Lagarde^b, Andrea Balocchi^b, Xavier Marie^b, Thomas Blon^b, Pascal Puech^c, Romain Bodeux^{d,e}

^a Université de Toulouse, CNRS-UPS-INPT, CIRIMAT, 118 Route de Narbonne, 31062 Toulouse, France

^b Université de Toulouse, INSA-CNRS-UPS, LPCNO, 135 Avenue Rangueil, 31077 Toulouse, France

^c Université de Toulouse, CNRS, CEMES, 29 rue Jeanne Marvig, 31055 Toulouse Cedex 4, France

^d EDF R&D, 6 quai Watier, 78400 Chatou Cedex, France

^e IRDEP, Institut de Recherche et Développement de l'Energie Photovoltaïque, 6 quai Watier, 78400 Chatou Cedex, France

ARTICLE INFO

Keywords:

Gas-temple
Nanocrystals
Kesterite
Solar cells
Ink process

ABSTRACT

A high-temperature gas-templating strategy is proposed to synthesize $\text{Cu}_2\text{ZnSnS}_4$ (CZTS) nanocrystals for all-aqueous solar inks. Our gas templating process route involves the in-situ generation and stabilization of nanosized gas bubbles into a molten KSCN-based reaction mixture at 400 °C. Chemical insights of the templating gas process are provided such as the simultaneous formation of gas bubbles and CZTS nuclei highlighting the crucial role of the nucleation stage on the sponge and resulting nanocrystals properties. The high porosity displayed by the resulting CZTS nanocrystals facilitates their further post-fragmentation, yielding individualized nanocrystals. The advantages of our high temperature gas templating route are illustrated by the following: (i) the low defect concentration displayed by the highly crystalline nanocrystals, (ii) the synthesis of CZTS nanocrystals displaying S^{2-} polar surfaces after ligand exchange. The good photoluminescence properties recorded on the pure CZTS nanocrystals reveal potential for exploration of new complex chalcogenide nanocrystals useful for various applications including photovoltaics and water splitting. Here we demonstrate that using these building blocks, a CZTS solar cell can be successfully fabricated from an environment-friendly all-aqueous ink.

1. Introduction

Chalcogenide nano-objects (e.g. CdS, PbS, ZnS, CuInS_2 , etc.) have been proposed as promising building blocks [1–4] for technological applications in the fields of biomedical diagnosis [5], optoelectronics [6], thermoelectricity [7] or photovoltaics [8]. Exciting opportunities for both fundamental studies and innovative technologies in the fields of energy materials will emerge from the design and synthesis of new, complex, chalcogenide nanocrystals displaying high optoelectronic properties. In particular, semiconducting nanocrystals displaying low defect concentration have received increased attention in the fields of photovoltaics [8] and hydrogen production [9]. However, structure crystallization of complex chalcogenide compounds generally occurs at higher temperatures [10,11] compared to single cation chalcogenides. As an example, quaternary chalcogenide $\text{Cu}_2\text{ZnSnS}_4$ (CZTS) [10], or doped CZT (S,Se) compounds such as

$\text{Cu}_{2-x}\text{Cd}_{1-x}\text{SnS}_4$ [11,12], $\text{Cu}_2\text{ZnSn}_{1-x}\text{In}_x\text{Se}_4$ [13], have been recently proposed.

Although some synthetic procedures describing the fabrication of these complex chalcogenide nanocrystals have been already proposed [14,15], the synthesis of these chalcogenide nanocrystals showing high chemical homogeneity, high crystallinity and low electronic-defect concentration, as required for optoelectronic or photovoltaic applications, still represents a challenge. In particular, CZTS solar cells fabricated by the ink process were mainly developed in apolar toxic solvents such as hexanethiol and involving oleyl-amine capped CZTS nanocrystals. For environmental considerations, design of an ink process in an all-aqueous CZTS nanocrystals dispersion is of a great interest [16,17]. In this context, synthesis of CZTS nanocrystals displaying low defect concentration and polar surfaces is highly desirable.

A strategy to synthesize highly homogeneous, crystalline complex building blocks is to design a high temperature synthetic route [18,19]. Indeed, high temperature facilitates both the achievement of crystallinity and defects annealing while repelling impurities to the outer surface of the nanocrystals. Nevertheless, high temperature formation of these nanocrystals remains a key

* Corresponding author. Tel.: +33 5 6155 6115; fax: +33 5 6155 6163.

E-mail address: chane@chimie.ups-tlse.fr (J.-Y. Chane-Ching).

issue because of the strong driving force available both for sintering and coarsening leading to irreversible growth and coalescence of the starting nanoparticles.

In this paper, we report on an innovative high temperature route ($T=400\text{--}450\text{ }^\circ\text{C}$) for the fabrication of non-aggregated, highly crystalline CZTS nanocrystals involving a gas template generated in-situ from molten KSCN. Our process route is operating both at high temperature and in a high supersaturation regime yielding nanosized CZTS crystals possessing a highly crystallized core. Removal of the SCN^- species, localized at the nanocrystal outer surface, is achieved through the $\text{S}^{2-}/\text{SCN}^-$ surface post-exchange [20]. Advantages of the gas templating process route are illustrated by the good optoelectronic properties as revealed from photoluminescence data recorded on CZTS nanocrystals films. More interestingly, by combining CZTS nanocrystals synthesized from this gas templating route with optimized forming and annealing procedures, first solar cells processed from an all-aqueous nanocrystals ink were successfully fabricated with device efficiency up to 2.5%.

2. Experimental section

2.1. CZTS nanocrystals synthesis

Metallic salts (CuCl , $2\text{H}_2\text{O}$ (Sigma Aldrich), ZnCl_2 (Sigma Aldrich), $\text{SnCl}_4 \cdot 5\text{H}_2\text{O}$ (Fischer Scientific)) were dissolved in EtOH. An intimate solid mixture of these salts is achieved after solvent elimination by roto-evaporation at $80\text{ }^\circ\text{C}$. Solid KSCN (Fluka) was then added at room temperature to the metallic salts and homogeneously mixed using a solid vortex mixer yielding a solid precursor. These precursors transferred into a SiO_2 container were heat-treated under Ar controlled atmosphere. Reaction mixtures were maintained at various temperatures ranging from $T=300\text{ }^\circ\text{C}$ to $550\text{ }^\circ\text{C}$ with various times duration t , $2\text{ h} < t < 32\text{ h}$. The temperature ramp rate was varied from $1\text{ }^\circ\text{C}/\text{min}$ to $3\text{ }^\circ\text{C}/\text{min}$. *Caution: Possible $(\text{CN})_{2\text{gas}}$ formation requires an appropriate trapping equipment to prevent inhalation.* After cooling to room temperature, a significant volume increase of the reaction mixtures was observed and the porous solids (CZTS–KC–KSCN sponges) were collected. The KSCN was removed from the composite sponges by subsequent washing in deionized water and EtOH, yielding a black solid (CZTS aggregates) which was finally dried at room temperature in air. After ball milling in ethanol, a ligand exchange involving S^{2-} anions [20] was as performed using an aqueous $(\text{NH}_4)_2\text{S}$ solution, yielding an aqueous CZTS dispersion after size selection by centrifugation at 6000 rpm.

2.2. CZTS solar cells fabrication

CZTS nanocrystals films were prepared by dip coating from an all aqueous dispersion (40 g l^{-1} CZTS) using a multi-step procedure on a Glass/Mo substrate. Typically, 18 layers were successively deposited at 100 mm min^{-1} to achieve a $2\text{ }\mu\text{m}$ crack-free film. After room temperature drying of the films in air atmosphere, the films and Se powder (125 mg) were annealed on a graphite susceptor under a quartz jell bar at $580\text{ }^\circ\text{C}$ for 15 min. The complete device stack was Glass/Mo/CZTSSe/CdS/i-ZnO:ZnO:Al. CdS was applied via chemical bath deposition while i-ZnO and ZnO:Al were deposited by sputtering.

2.3. Characterizations

2.3.1. BET isotherm

Surface area and pore size distribution of the CZTS aggregates after H_2O washing were measured by nitrogen adsorption/

desorption isotherms using a Micromeritics ASAP 2000 system at 77 K . The sample was degassed at 473 K under vacuum for 8 h before analysis. The surface area was measured using the Brunauer–Emmet–Teller (BET) model for relative pressure in the range 0.05–0.30 and the distribution of pore dimensions was calculated using the Barret–Joyner–Halenda (BJH) model.

2.3.2. Raman spectroscopy

Micro-Raman measurements were performed using a Horiba Jobin Yvon XPlora equipped with an Olympus microscope. A $50\times$ objective and low laser power ($0.01 P_0$, $P_0=40\text{ mW}$ at 785 nm) have been used to avoid any thermal effects due to laser heating. With $0.1P_0$ laser power, downshift of Raman bands due to heating was observed while the spectra remain identical with 0.1%. The focused spot diameter on the samples was $\sim 1\text{ }\mu\text{m}$ leading to an excitation power of $0.5\text{ mW}/\mu\text{m}^2$.

2.3.3. FEG-SEM-TEM

The KSCN–CZTS sponges were imaged by a FEG-SEM and the relative atomic composition of the sponges were determined using energy dispersive spectroscopy (EDS). Specimens for low magnification transmission electron microscopy (TEM) and high resolution transmission electron microscopy (HRTEM) were obtained by drying droplets of a CZTS sample from an ethanolic dispersion onto a 300 mesh Cu grid, coated with a Lacey carbon film. TEM images were taken at an accelerating voltage of 100 kV on a JEM 1011. HRTEM images were obtained on a JEOL JEM 2100F at an accelerating voltage of 200 kV .

2.3.4. Photoluminescence

Time-resolved and time-integrated photoluminescence experiments were performed using a mode-locked Ti:Sa laser with 1.2 ps pulse duration and 80 MHz repetition frequency, at a wavelength $\lambda=760\text{ nm}$ and average power $P_{\text{aver}}=3\text{ mW}$, focussed to a $50\text{ }\mu\text{m}$ diameter spot. The PL dynamics were recorded with a S1 photocathode Hamamatsu synchroscan Streak Camera C 5680 with 10 ps overall time resolution.

3. Results and discussion

Heat treatment under N_2 of $\text{CuCl}\text{--}\text{ZnCl}_2\text{--}\text{SnCl}_4\text{--}\text{KSCN}$ mixtures with $(\text{Cu}^+:\text{Zn}^{2+}:\text{Sn}^{4+}:\text{SCN}^-)=(2:1:1:r)_{\text{molar ratio}}$, $7.5 \leq r \leq 30$ at temperatures ranging from $325\text{ }^\circ\text{C}$ to $500\text{ }^\circ\text{C}$ during 16 h produces after cooling at room temperature sponges (Fig. 1a) containing CZTS nanocrystals and reaction by-products, namely KCl and KSCN. Our high temperature process involving an in-situ generated gas offers the advantage to yield, after KSCN–KCl removal, loosely-packed CZTS aggregates as shown from a TEM investigation (Fig. 1b). The loose packing of the CZTS aggregate favors the formation of 30 nm , perfectly individualized CZTS nanocrystals (Fig. 1c) achieved by post-fragmentation and selection. More interestingly, the gas template preserves the low compactness of the CZTS aggregates during high temperature aging stage (16 h at $400\text{ }^\circ\text{C}$), required for the full crystallization of the CZTS nanocrystals as shown from a Raman investigation (Fig. 1d).

3.1. Identification of the in-situ generated gas and reaction pathways

Control experiments performed under similar experimental conditions $(\text{Cu}:\text{Zn}:\text{Sn}:\text{S})=(2:1:1:15)_{\text{molar}}$, $T=400\text{ }^\circ\text{C}$ during 16 h using Cu_2O , ZnO , and SnO_2 as metal sources yield CZTS particles, without any volume expansion of the reaction mixtures, consistent with the reaction $\text{Cu}_2\text{O}+\text{ZnO}+\text{SnO}_2+4\text{KSCN}=\text{Cu}_2\text{ZnSnS}_4+4\text{KCNO}$ [21]. These observations demonstrates the crucial role of the metallic salts addition in the KSCN/CZTS sponges formation.

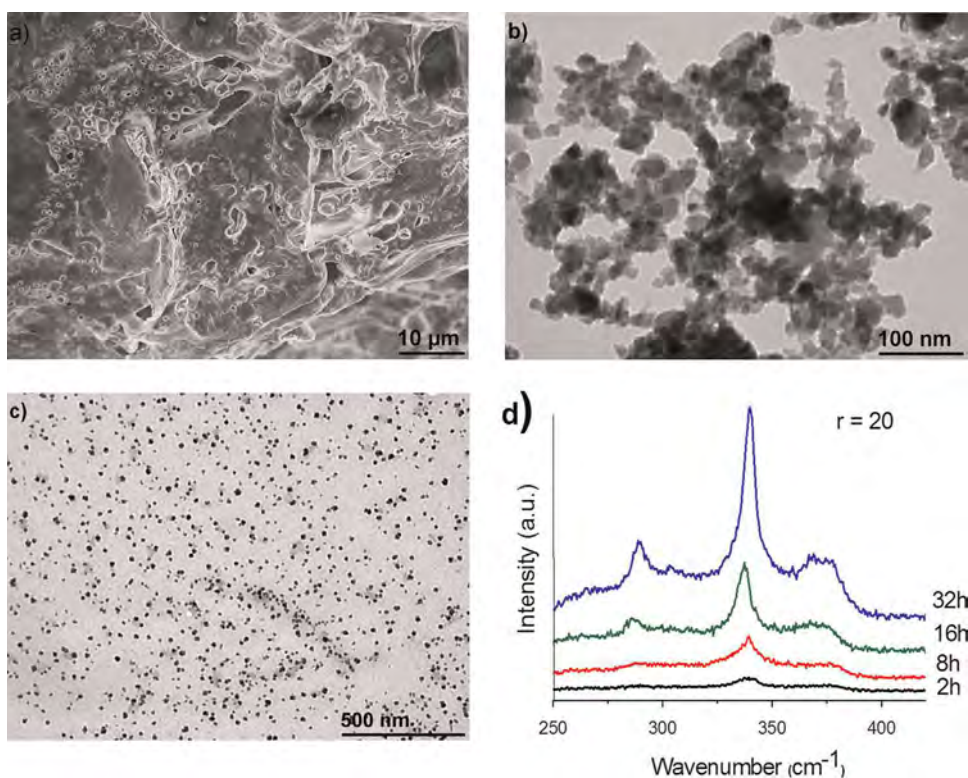


Fig. 1. (a) FE-SEM image of fractured KSCN-KCl-CZTS sponge showing pores sizes d , $10 \mu\text{m} < d < 1 \mu\text{m}$. Sample prepared at $(\text{Cu}:\text{Zn}:\text{Sn}:\text{SCN})=(2:1:1:20)$, $400 \text{ }^\circ\text{C}$, 16 h , $\nu=1 \text{ }^\circ\text{C}/\text{min}$. (b) Typical TEM image of CZTS aggregates obtained after KSCN-KCl removal, showing porous architecture. Loosed-packed aggregates are formed from primary crystallites of 30 nm and pores with sizes d , $\text{nm} < d < \mu\text{m}$. (c) TEM image of perfectly individualized CZTS nanocrystals after fragmentation by ball milling and size selection performed by ultracentrifugation at 4500 rpm . (d) Raman spectra recorded on CZTS nanocrystals showing two main peaks at 286 and 337 cm^{-1} (A_1 symmetry modes). A better short distance order is observed for samples synthesized at longer aging times at $400 \text{ }^\circ\text{C}$. $(\text{Cu}:\text{Zn}:\text{Sn}:\text{SCN})=(2:1:1:20)$, $\nu=1 \text{ }^\circ\text{C}/\text{min}$. The curves have been displaced vertically for clarity.

With the objective to identify the in-situ formed gas, we performed chemical analysis of the reaction byproducts. No significant consumption of the chloride anion during the CZTS formation reaction was revealed from chemical analysis of the aqueous solutions recovered from dissolution of the sponges. Thus, CZTS-KSCN-KCl sponge formation does not arise from oxidation of the chloride anion into Cl_2 gas. Interestingly, the sponges' formation occurs at temperatures around the onset of CZTS formation as shown from an XRD investigation of samples prepared at various temperatures (see Supporting Information, Fig. S1). This suggests that the in-situ generation of gas is associated with the S^{2-} anion formation. In addition, syntheses performed at $(\text{Cu}^+:\text{Zn}^{2+}:\text{Sn}^{4+}:\text{SCN}^-)=(2:1:1:r)_{\text{molar}}$, with increased r values, yield large volume expansions (Fig. 2). Again, this larger volume expansion observed with dilution of $[\text{Cu}]$, $[\text{Zn}]$ and $[\text{Sn}]$ concentrations can be associated to the formation of S^{2-} in a larger concentration. A reaction pathway to the sponges' formation can thus be proposed. In a first stage, the decomposition of SCN^- anion at temperatures T , $T > 275 \text{ }^\circ\text{C}$ occurs as already reported [20], with S formation: $\text{SCN}^- = \text{S} + \text{CN}^-$. Indeed, presence of sulfur traces was observed on X-ray diffractograms performed on the solids collected in the cold part of the gas circuit. In a second stage, formation of S^{2-} anions required for the $\text{Cu}_2\text{ZnSnS}_4$ precipitation is achieved from the previously reported following oxydo-reduction reactions [22] (i) $\text{S} + 2\text{CN}^- = \text{S}^{2-} + (\text{CN})_2$ gas or/and (ii) $\text{S} + 2\text{CN}^- = \text{S}^{2-} + 2\text{C} + \text{N}_2$ gas. In our experimental conditions, our reaction pathway is confirmed by the presence of carbon in the as-synthesized CZTS nanocrystals as shown by a Raman spectroscopy investigation (Fig. S2). Note that in a control experiment, thermal decomposition of KSCN alone did not produce any gas evolution

confirming that the N_2 (and eventually $(\text{CN})_2$) gas formation is thus closely associated to the CZTS precipitation.

3.2. Kinetics of formation of the gas bubbles and their stabilization into the molten salt

A large range of pores exhibiting sizes ranging from the millimeter to the nanometer scale was observed on optical and electronic microscopy images recorded on the KSCN-KCl-CZTS sponges (Fig. 1). This indicates reasonably good stabilization and trapping of the gas bubbles respectively during the aging and cooling stages. Formation kinetic of bubbles was investigated on samples yielding large volume expansion $((\text{Cu}^+:\text{Zn}^{2+}:\text{Sn}^{4+}:\text{SCN}^-)_{\text{mole}}=(2:1:1:r)$, $r=20$ and $\nu=6 \text{ }^\circ\text{C}/\text{min}$, ν =temperature ramping rate) and recovered at various stages of the process. A nearly constant sponge volume was determined as well on the sponges collected just after the first stages of nucleation-growth (1 min , $400 \text{ }^\circ\text{C}$), as on samples recovered after various aging times, up to 16 h at $400 \text{ }^\circ\text{C}$ (Fig. 3). In order to better specify the gas volume generated during the aging step (16 h at $400 \text{ }^\circ\text{C}$), a control experiment performed in identical experimental conditions, but including a degassing stage under vacuum just after the first stage of nucleation-growth (1 min , $400 \text{ }^\circ\text{C}$) showed a sponge volume decrease of 50% (Fig. 3). These observations demonstrate both the formation of bubbles in large quantity during the first step of nucleation-growth and their stabilization into the reaction mixture during the aging period at $400 \text{ }^\circ\text{C}$. Besides, this suggests a low rate of gas bubbles coalescence into the molten salt. Lastly, these results are consistent with the proposed reaction pathway concerning the in-situ gas generation. Indeed, gas generation is activated by the S^{2-} anion formation required from the CZTS

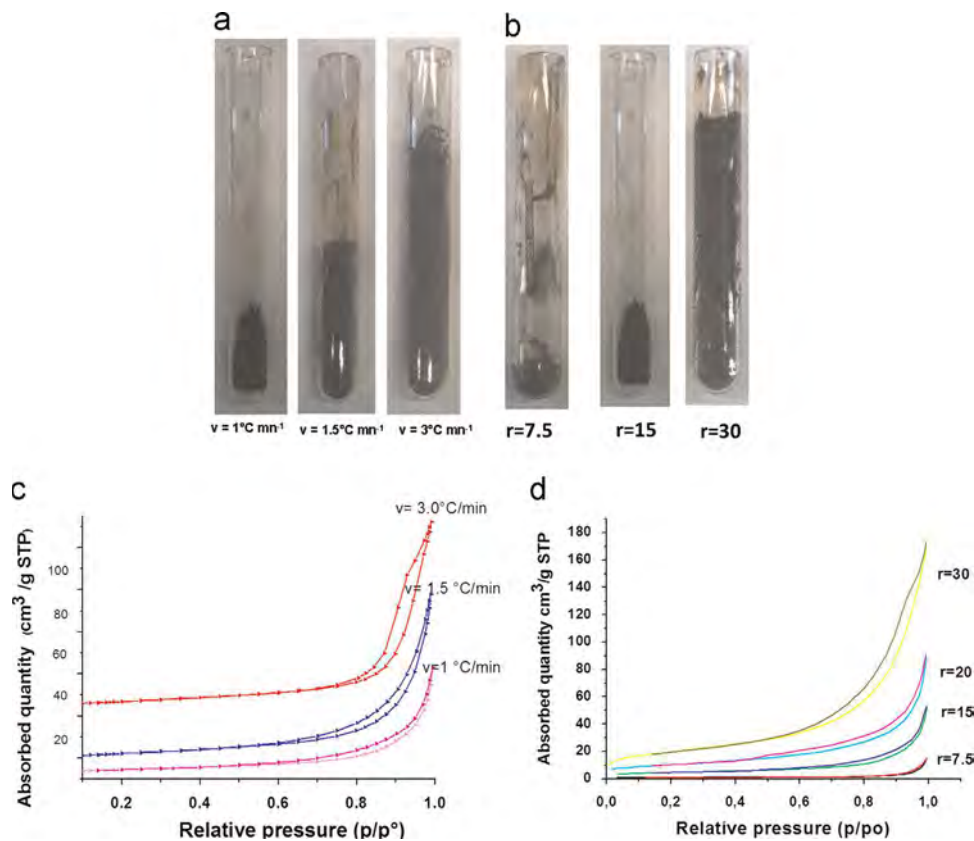


Fig. 2. (a) Photographs of CZTS/KSCN sponges prepared at increased v values, v = temperature ramp rate in $^\circ\text{C}/\text{min}$. ($r = 15$, $T = 400^\circ\text{C}$, 16 h). (b) Photographs of CZTS/KSCN sponges prepared at increased r values, r = KSCN moles ($T = 400^\circ\text{C}$, 16 h, $v = 1^\circ\text{C}/\text{min}$). (c) Absorption-desorption isotherms recorded on CZTS aggregates prepared at various temperature ramp rates, v , $T = 400^\circ\text{C}$, 16 h. ($\text{Cu}:\text{Zn}:\text{Sn}:\text{S}$) = (2:1:1:20). (d) Absorption-desorption isotherms recorded on CZTS aggregates prepared at various r , r = KSCN compositions. The adsorption-desorption curves have been displaced vertically for clarity.

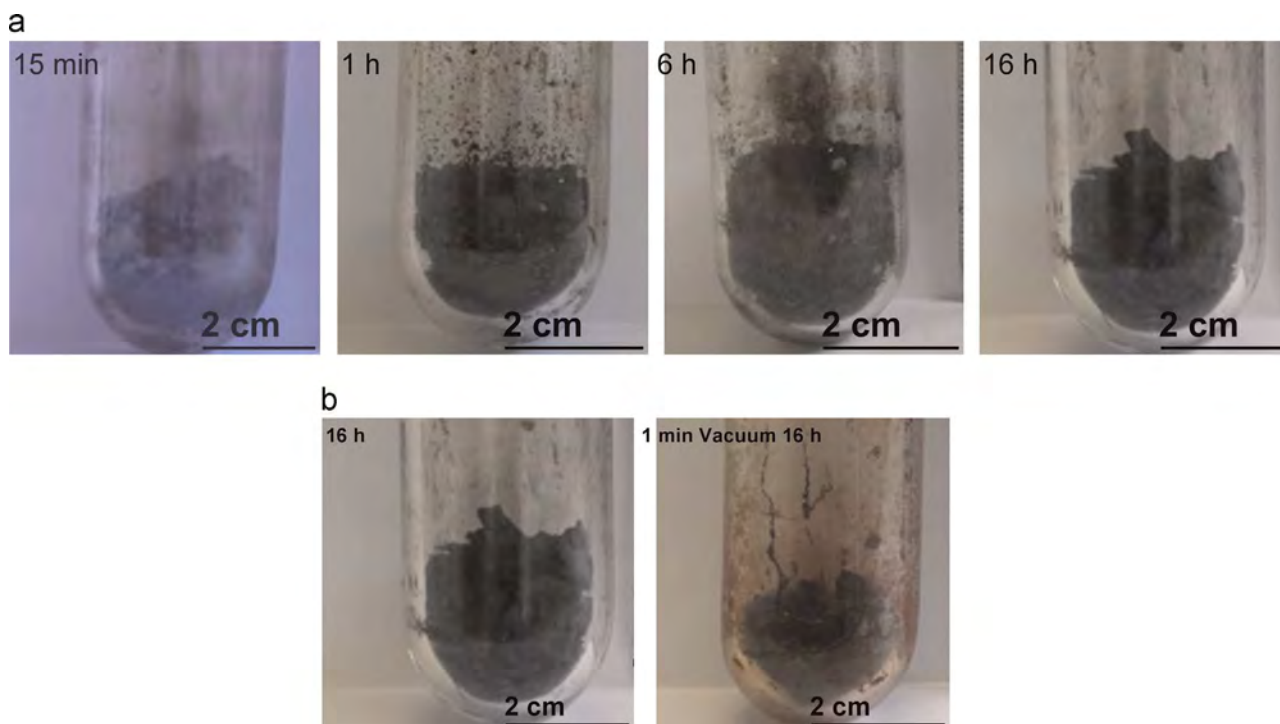


Fig. 3. (a) Photographs of KSCN-KCl-CZTS sponges recovered at various stages of the process illustrating the kinetic of formation of the gas bubbles into the molten reaction mixture. ($\text{Cu}:\text{Zn}:\text{Sn}:\text{KSCN}$) = (2:1:1:20), at $T = 400^\circ\text{C}$, and $v = 6^\circ\text{C}/\text{min}$. A nearly constant sponge volume is observed for aging time up to 16 h. (b) Photograph of KSCN-KCl-CZTS sponge recovered in a control experiment involving a degassing stage ($t = 15$ min vacuum) just after the first stage of nucleation growth showing a clear decrease of the sponge volume compared to a reference sample synthesized in similar conditions. ($\text{Cu}:\text{Zn}:\text{Sn}:\text{KSCN}$) = (2:1:1:20), at $T = 400^\circ\text{C}$, 16 h and $v = 6^\circ\text{C}/\text{min}$.

precipitation which mainly occurs during the first stages of the CZTS formation.

3.3. Sponge properties are dictated by the first stages of nucleation-growth

To fully demonstrate the key-role of the first stages of nucleation-growth on the sponge properties, samples were synthesized at various temperature ramping rates ($0.5\text{ }^{\circ}\text{C}/\text{min} < \nu < 6.0\text{ }^{\circ}\text{C}/\text{min}$) and collected just after the onset of the aging stage (1 min at $400\text{ }^{\circ}\text{C}$). Although the generated gas volumes should be theoretically identical for experiments performed at a constant number of CZTS moles, samples prepared in higher super-saturation regimes yield higher porous volumes (Fig. S3). Indeed, an approximately 1.5 fold increase was observed for the CZTS-KCl-KSCN sponge volume formed in similar conditions of composition ((Cu:Zn:Sn:SCN)=(2:1:1:15), $T=400\text{ }^{\circ}\text{C}$) but at a higher ramp rate, $\nu=3.0\text{ }^{\circ}\text{C}/\text{min}$, compared with the sample prepared at low temperature ramping rate, $\nu=1.0\text{ }^{\circ}\text{C}/\text{min}$. In another set of experiments performed at constant number of CZTS moles, larger volume expansions were also observed for samples prepared with dilution of metallic salts concentrations (increased r values) and recovered after the first stages of nucleation-growth ($t=1\text{ min}$, $400\text{ }^{\circ}\text{C}$). Increase of sponge volumes of these samples is attributed to the more important gas emission associated to the S^{2-} anions formation arising in larger concentration required by the CZTS precipitation in diluted metallic cations reaction mixtures. Note that in these diluted reaction mixtures, gas bubbles are generated in larger proportion very close to the CZTS nuclei, but at large inter-nuclei distances due to the dilution.

For these two sets of experiments, the large volume expansions recorded after the first stages of nucleation-growth are preserved all along the aging stage at $400\text{ }^{\circ}\text{C}$ during 16 h (Fig. 2), highlighting the crucial role of the first stages of nucleation-growth on the properties control both of sponges and of the resulting CZTS aggregates.

3.4. A gas templating process route

Control of the sponges properties was achieved in the first stages of CZTS precipitation, both by variation of CZTS nanocrystal nucleation rates (Fig. 2a) or by CZTS formation in diluted reaction mixtures (Fig. 2b). Fine inspection of the corresponding KSCN-KCl-CZTS sponges by Hg porosimetry reveals that samples exhibiting a large volume expansion also possess a large porous volume of (sub)-micronic pores ($D < 1.5\text{ }\mu\text{m}$) with pores volume fraction Φ_p , up to 45% (Table 1). Interestingly, with regard to the global pore population, these samples also display the largest proportion of (sub)-micronic size pores (Fig. 4). Concerning samples prepared at high super-saturation regimes, high sponge volume expansions could thus be attributed in parallel to the high number of CZTS nuclei formation, to the concomitant generation of a higher number of smaller size gas bubbles. Because the growth and coalescence of gas bubbles in the molten KSCN were previously shown to display a low kinetic, these small size bubbles yield later the observed larger proportion of (sub)-micronic pores. For the samples prepared in diluted reaction mixtures, the large volume expansions probably result from the high bubbles volume fraction generated in the vicinity of the CZTS nuclei. In this later case, bubbles coalescence is delayed because of the high inter-nuclei distance. In these two set of experiments, large sponge volume expansions could thus be ascribed to the simultaneous generation of a high volume fraction of small size gas bubbles in the nearby vicinity of CZTS nuclei.

After removal of the reaction by-products, a Brunauer-Emmett-Teller (BET) investigation shows that the corresponding

Table 1

Textural characteristics of KSCN-KCl-CZTS sponges and corresponding CZTS aggregates prepared at $T=400\text{ }^{\circ}\text{C}$ showing a dependence of pore volume fraction of CZTS aggregates on the sponges porosity arising from pores in the (sub)-micronic range. Porous characteristics of KSCN-KCl-CZTS sponges and of CZTS aggregates were respectively determined from Hg porosimetry and BET adsorption curves. Primary crystallite sizes (D_{cryst}) were determined from TEM images.

16 h $400\text{ }^{\circ}\text{C}$	$V=1\text{ }^{\circ}\text{C}/\text{min}$ $r=7.5$	$r=15$	$r=20$	$V=3\text{ }^{\circ}\text{C}/\text{min}$ $r=20$
KSCN-KCl-CZTS sponges				
V_p (cm^3/g)	0.35	0.55	0.70	0.70
ϕ_v	0.35	0.41	0.45	0.45
D pores (μm)	1.5	1	1	1.2
CZTS aggregates				
V_p (cm^3/g)	0.02	0.08	0.14	0.265
ϕ_v	0.09	0.28	0.40	0.56
SS (m^2/g)	3	16	36	58
D_{cryst} (nm)	30	30	30	30

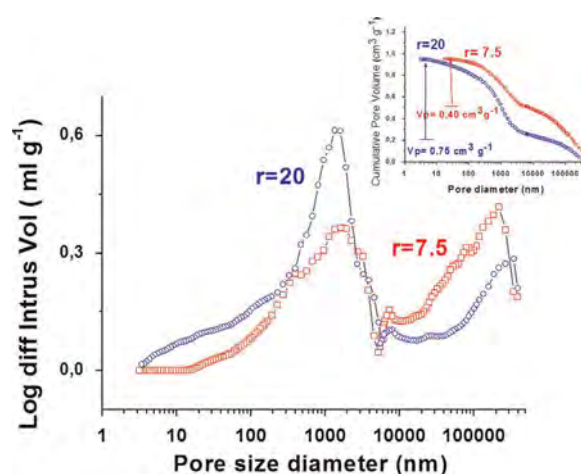


Fig. 4. Pores distribution of KSCN-KCl-CZTS samples showing a larger proportion of sub-(micronic) pores compared to the pores global population for the sample displaying higher volume expansion ($r=20$). Inset: Cumulative pore volume determined by Hg porosimetry showing that the sample exhibiting the larger proportion of sub-(micronic) pores also display the higher (sub)-micronic pore volume.

CZTS aggregates prepared from a series of sponges displaying increased volume expansions exhibit a continuous variation of the porosity at the nanometer scale. Fig. 2c and d compares BET absorbed volumes of CZTS aggregates obtained from sponges prepared at various nucleation rates or at various metallic salt dilutions (high r values). In these two sets of experiments, highly porous CZTS aggregates with BET nanosized porosity up to 56% were obtained from KSCN-KCl-CZTS sponges possessing higher pore volume (Table 1). These results reveal that the porous architecture of the CZTS aggregates is thus strongly dependent of the volume fraction of (sub)-micronic gas bubbles formed inside the molten reaction mixture.

In contrast to the millimetric size bubbles usually observed by gas bubbling into a molten salt [23], the reasonable high volume fraction of submicronic pores along the ellipsoidal morphology displayed by some micronic pores observed on our sponges (Fig. 5a), indicate a slow kinetic of bubbles growth and their stabilization into the reaction mixture. This bubbles stabilization probably arises from a high interaction between the gas bubbles and the CZTS nanocrystals surfaces. Indeed, high magnification FE-SEM images recorded on the fractured KSCN-KCl-CZTS sponges (Fig. 5b) clearly show the presence of gas/CZTS nanocrystal along gas/KSCN interfaces at pores periphery. We thus propose that CZTS

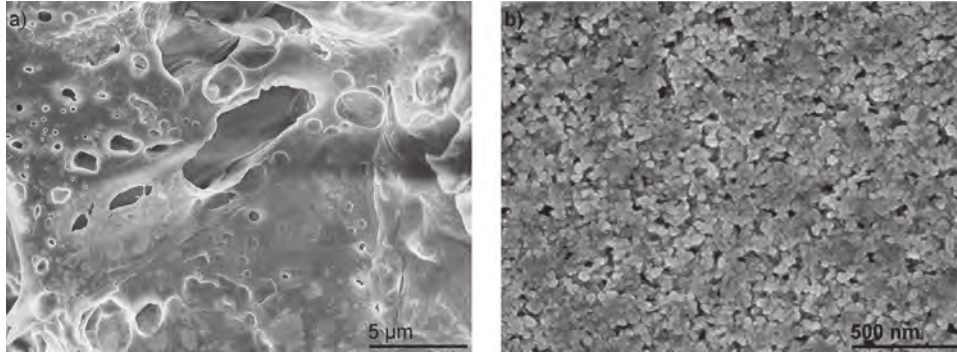


Fig. 5. (a) FE-SEM image of a fractured KSCN-KCL-CZTS sponge showing a pseudo ellipsoidal morphology of micronic pores. ($T=400\text{ }^{\circ}\text{C}$, 16 h. $(\text{Cu}:\text{Zn}:\text{Sn}:\text{S})=(2:1:1:20)$, $\nu=3\text{ }^{\circ}\text{C}/\text{min}$). (b) MEB-FEG high magnification image of a KSCN-KCL-CZTS fractured sponge showing pores/KSCN and pore/CZTS nanocrystal interfaces. These interfaces can be differentiated by the less-defined morphology of CZTS nanocrystals observed in domains containing KSCN.

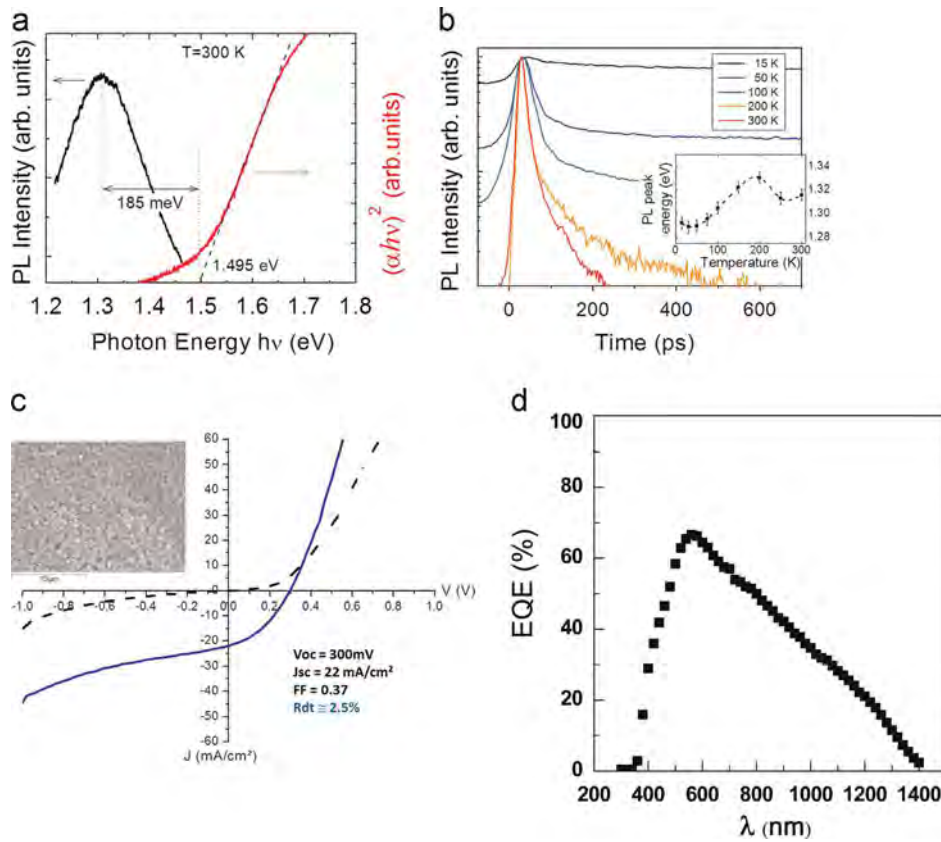


Fig. 6. (a) PL spectrum measured at $T=300\text{ K}$ on CZTS films after annealing at $550\text{ }^{\circ}\text{C}$ under N_2 . The dependence of $(\alpha h\nu)^2$ on photon energy where α is the absorption coefficient is also plotted showing a Stokes shift of 185 meV . (b) Corresponding photoluminescence kinetics recorded at various temperatures showing long decay times at low temperature, characteristics of Donor Acceptor Pair transitions. The kinetics has been displaced for clarity. Inset: PL peak energy as a function of the temperature. (c) Light and dark $J(V)$ characteristics under simulated 1 sun AM 1.5 G of a Glass/Mo/CZTS/CdS/ZnO;ZnO:Al solar cell processed from an all-aqueous ink and annealed at $580\text{ }^{\circ}\text{C}$ 15 min under PSe. Inset: Top view SEM image of annealed CZTS(Se) film showing large grains up to the micrometer. (d) EQE spectrum of the CZTS(Se) device fabricated from the aqueous CZTS nanocrystals ink.

nanocrystals probably act as solid surfactants in molten KSCN, stabilizing gas bubbles inside the molten salt, in the same way as solid inorganic particles are known to stabilize liquid droplets in biphasic emulsions [24,25]. All these observations show that the CZTS aggregate properties such as its porosity could be controlled by the gas template, particularly by a fine-tuning of the size and volume fraction of the gas bubbles generated in the nearby vicinity of the CZTS nuclei.

3.5. Nanocrystals properties

The optoelectronic properties and the role of defects in the non-doped CZTS material were investigated by absorption, time-integrated and time-resolved photoluminescence (PL) spectroscopy on films prepared from CZTS nanoparticles and post calcined at $550\text{ }^{\circ}\text{C}$ under N_2 atmosphere. Fig. 6a presents the absorption and PL spectra at room temperature. The absorption

shows a bandgap energy $E_g \approx 1.5$ eV at $T=300$ K consistent with the values reported in the literature ranging from 1.45 to 1.6 eV [26]. The PL peak energy is measured at 1.315 eV at $T=300$ K, which is significantly smaller than the bandgap. This demonstrates that the main radiative recombination channel does not occur between free electrons and free holes in the conduction and valence bands respectively. The observation of an increase of the PL peak energy, from 1.28 eV at 15 K to 1.315 eV at 300 K (inset of Fig. 6b) together with the measurement of very long PL decay times (> 5 ns) at low temperature (Fig. 6b), are characteristic of Donor–Acceptor Pair (DAP) transitions. These are associated with the presence of a high density of intrinsic point defects yielding local deviations in the distribution of donors (Zn_{Cu}) and acceptors (V_{Cu}), and introducing fluctuations in the band structure [27,28]. The reasonable PL intensity recorded at 300 K indicates that our highly crystallized CZTS nanocrystals possess a rather low non-radiative defect concentration. This is consistent with a PL decay time of ~ 50 ps at room temperature (Fig. 6b) and demonstrates that the optoelectronic properties of our CZTS films are comparable with photovoltaic quality CZTS materials.

Use of a gas-template has the advantage to minimize pollutants incorporation into the CZTS nanocrystals in a high temperature process route. With the objective to take full advantage of the good optoelectronic properties previously shown, a surface purification of the as-synthesized CZTS nanocrystals exhibiting SCN^- -capped surfaces (Fig. S4) was performed by a S^{2-}/SCN^- ligand exchange. The highly charged, polar surfaces of the resulting S^{2-} -CZTS capped nanocrystals has facilitated the fabrication of an environment-friendly, all-aqueous, CZTS ink. Due to the high interfacial tension existing in a wet aqueous nanocrystals film, films of thickness larger than 400 nm form with a fully interconnected crack network. In contrast, using a layer by layer deposition process, a crack-free film of a final thickness of around 2 μm was produced by consecutively depositing 110 nm thick coatings (18 times) (Fig. S5). Complete carbon purification of nanocrystals films (Fig. S2) was achieved by implementing a purification step (500 °C 30 min, 125 mg Se) in our annealing process. Combined with optimized selenization procedure (580 °C, 125 mg Se), a significant grain growth was obtained on annealed pure CZTSe films with CZTSe grain size up to 1 μm (Fig. 6c). More interestingly, unlike the use of non-well crystallized nanoparticles [29], use of highly crystallized building blocks offers the advantage to yield CZTSe films without formation of any secondary phase such as ZnS(Se) as shown from a Raman spectroscopy kinetic investigation (Fig. S6). By taking benefit of these gas-templated CZTS nanocrystals possessing high optoelectronic properties and polar surfaces, we have thus successfully fabricated first CZTS solar cells from an all aqueous ink, with device efficiencies of 2.5% (Fig. 6c). Examination of the EQE data shows a peak photocurrent efficiency of 67% at 560 nm (Fig. 6d). This relatively low value could arise from a short diffusion length of minority carriers or from a slight sulfur gradient of the absorber. For wavelengths below 560 nm, losses of photocarriers are mainly due to the front contact ZnO/CdS. At longer wavelengths, i.e. between 560 nm and 1400 nm, the observed gradual decrease of the photocurrent could be ascribed to the reduced light absorption in this spectral region caused by a less than optimal film thickness of the absorber layer which was 1.0 μm . The observed photocurrent decay in the infrared domain may also result from defect-related recombination losses. From these results, we anticipate that higher conversion efficiencies should be achieved with an increase of the absorber thickness ($> 1 \mu m$) and with an improved control of the annealing conditions (optimization of the annealing atmosphere to minimize possible absorber chemical degradation).

4. Conclusions

A high-temperature, gas templating process route is proposed yielding complex Cu_2ZnSnS_4 chalcogenide nanocrystals. Stabilization of in-situ generated gas bubbles in a molten reaction mixture is achieved via CZTS nanocrystal surfaces/gas interactions. The gas template is shown to control the CZTS aggregates porosity. Moreover, the gas template facilitates the CZTS nanocrystal full crystallization while preserving their nanometer size. Coupled to a S^{2-} ligand surface exchange, this synthetic methodology enables the preparation of highly crystallized chalcogenide nanocrystal cores displaying polar surfaces. We have taken benefit of the good optoelectronic properties of these nanocrystals to develop an environment-friendly film forming process. First CZTS solar cells were thus successfully fabricated from all-aqueous CZTS inks with device efficiencies up of 2.5%. This gas templating strategy offers a general process route for preparing a broad class of highly crystalline, complex, semiconducting chalcogenides. These highly crystalline chalcogenide building blocks should be of great interest for films preparation in various applications such as H_2 production, CO_2 , photovoltaic or thermoelectric conversions.

Acknowledgments

We thank Lionel Bonneau (Baikowski Chimie) and Alain Seraphine (Region Reunion) for very helpful discussions. This work was partially supported by fundings from Region Reunion and NovACEZ ANR Project.

Appendix A. Supplementary material

Supplementary data associated with this article can be found in the online version at <http://dx.doi.org/10.1016/j.solmat.2015.06.009>.

References

- [1] W.U. Huynh, J.J. Dittmer, A.P. Alivisatos, Hybrid nanorod-polymer solar cells, *Science* 295 (2002) 2425–2427.
- [2] J. Tiang, S. Hinds, S.O. Kelley, E.H. Sargent, Synthesis of colloidal $CuGaSe_2$, $CuInSe_2$, and $Cu(InGa)Se_2$ nanoparticles, *Chem. Mater.* 20 (2008) 6906–6910.
- [3] X. Zhong, R. Xie, Y. Zhang, T. Basche, W. Knoll, High-quality violet- to red-emitting ZnSe/CdSe core/shell nanocrystals, *Chem. Mater.* 17 (2005) 4038–4042.
- [4] J. Tang, E.H. Sargent, Infrared colloidal quantum dots for photovoltaics: fundamentals and recent progress, *Adv. Mater.* 23 (2011) 12–29.
- [5] J.M. Klostranec, W.C. Chan, Quantum dots in biological and biomedical research, *Adv. Mater.* 18 (2006) 1953–1964.
- [6] V.L. Colvin, M.C. Schlamp, A.P. Alivisatos, Light-emitting diodes made from cadmium selenide nanocrystals, *Nature* 370 (1994) 354–357.
- [7] C. Xiao, J. Xu, K. Li, J. Feng, J. Yang, Y. Xie, Superior phase transition in silver chalcogenide nanocrystals realizing optimized thermoelectric performance, *J. Am. Chem. Soc.* 134 (2012) 4287–4293.
- [8] A.G. Pattantyus-Abraham, I.J. Kramer, A.R. Barkhouse, X. Wang, G. Konstantatos, R. Debnath, L. Lavina, I. Raabe, M.K. Nazeeruddin, M. Gratzel, E.H. Sargent, Depleted-heterojunction colloidal quantum dot solar cells, *ACS Nano* 4 (2010) 3374–3380.
- [9] A.B. Laursen, S. Kegnaes, S. Dahl, Ib Chorkendorff, Molybdenum sulfides – efficient and viable materials photoelectrocatalytic hydrogen evolution, *Energy Environ. Sci.* 5 (2012) 5577–5591.
- [10] C. Steinhagen, M.G. Panthani, V. Akhavan, B. Goodfellow, B. Koo, B.A. Korgel, Synthesis of Cu_2ZnSnS_4 nanocrystals for use in low-cost photovoltaics, *J. Am. Chem. Soc.* 131 (2009) 12554–12555.
- [11] M.L. Liu, I.W. Chen, F.Q. Huang, L.D. Chen, Improved thermoelectric properties of Cu doped quaternary chalcogenides of $Cu_2CdSnSe_4$, *Adv. Mater.* 21 (2009) 3808–3812.
- [12] M. Ibanez, D. Cadavid, R. Zamani, N. Garcia-Castello, V. Izquierdo-Roca, W. Li, A. Fairbrother, J.D. Prades, A. Shavel, J. Arbiol, Composition control and thermoelectric properties of quaternary chalcogenide nanocrystals: the case of stannite $Cu_2CdSnSe_4$, *Chem. Mater.* 24 (2012) 562–570.

- [13] X.Y. Shi, F.Q. Huang, M.L. Liu, L.D. Chen, Thermoelectric properties of tetrahedrally bonded wide-gap stannite compounds $\text{Cu}_2\text{ZnSn}_{1-x}\text{In}_x\text{Se}_4$, *Appl. Phys. Lett.* 94 (2009) 122103.
- [14] S.C. Riha, B.A. Parkinson, A.L. Prieto, Solution-based synthesis and characterization of $\text{Cu}_2\text{ZnSnS}_4$ nanocrystals, *J. Am. Chem. Soc.* 131 (2009) 12054–12055.
- [15] O. Zaberca, A. Gillorin, B. Durand, J.Y. Chane-Ching, A general route to the synthesis of surfactant-free, solvent – dispersible ternary and quaternary chalcogenide nanocrystals, *J. Mater. Chem.* 21 (2011) 6483–6486.
- [16] P. Kush, S.K. Ujjain, N.C. Mehra, P. Jha, R.K. Sharma, S. Deka, Development and properties of surfactant-free water-dispersible $\text{Cu}_2\text{ZnSnS}_4$ nanocrystals: a material for low-cost photovoltaics, *Chem. Phys. Chem.* 14 (2013) 2793–2799.
- [17] J. Zhong, Z. Xia, C. Zhang, B. Li, X. Liu, Y.B. Cheng, J. Tang, One-pot synthesis of self-stabilized aqueous nanoinks for $\text{Cu}_2\text{ZnSn}(\text{S},\text{Se})_4$ solar cells, *Chem. Mater.* 26 (2014) 3573–3578.
- [18] G. Mialon, M. Gohin, T. Gacoin, J.P. Boilot, High temperature strategy for oxide nanoparticle synthesis, *ACS Nano* 2 (2008) 2505–2512.
- [19] J.Y. Chane-Ching, G. Martinet, P.J. Panteix, C. Brochard, A. Barnabe, M. Airiau, Size and morphology control of ultrafine refractory complex oxide crystals, *Chem. Mater.* 23 (2011) 1070–1077.
- [20] A. Nag, M.V. Kovalenko, J.S. Lee, W. Liu, B. Spokoyny, D.V. Talapin, Metal-free inorganic ligands for colloidal nanocrystals: S^{2-} , HS^- , Se^{2-} , HSe^- , Te^{2-} , HTe^- , TeS_3^{2-} , OH^- and NH_2^- as surface ligands, *J. Am. Chem. Soc.* 133 (2011) 10612–10621.
- [21] P. Bohac, V. Tanner, A. Gaemann, Crystallization of sulphides in KSCN melts, *Cryst. Res. Technol.* 17 (1982) 717–722.
- [22] A. Eluard, B. Tremillon, Propriétés physiques et électrochimiques en solution dans le thiocyanate de potassium fondu, formation de complexes cyanure, *J. Electroanal. Chem.* 13 (1967) 208–226.
- [23] S. Phongikaroon, R.W. Bezzant, M.F. Simpson, Measurements and analysis of oxygen bubble distributions in LiCl–KCl molten salt, *Chem. Eng. Res. Des.* 91 (2013) 418–425.
- [24] S. Jiang, Q. Chen, M. Tripathy, E. Luijten, K.S. Schweizer, S. Granick, Janus particle synthesis and assembly, *Adv. Mater.* 22 (2010) 1060–1071.
- [25] B.J. Park, D. Lee, Equilibrium orientation of nonspherical janus particles at fluid–fluid interfaces, *ACS Nano* 6 (2012) 782–790.
- [26] K. Wang, O. Gunawan, T. Todorov, B. Shin, S.J. Chey, N.A. Bojarczuk, D. Mitzi, S. Guha, Thermally evaporated CZTSS solar cells, *Appl. Phys. Lett.* 97 (2010) 143508-3.
- [27] I. Dirnstorfer, M. Wagner, D.M. Hoffmann, M.D. Lampert, F. Karg, B.K. Meyer, Characterization of $\text{Cu}_2\text{In}(\text{Ga})\text{Se}_2$ thin films, *Phys. Stat. Sol. A* 168 (1998) 163–175.
- [28] S.A. Schumacher, J.R. Botha, V. Alberts, Photoluminescence study of fluctuations potentials in thin layers of $\text{Cu}_2(\text{In}_{0.75}\text{Ga}_{0.25})(\text{S}_y\text{Se}_{1-y})_2$, *J. Appl. Phys.* 99 (2006) 063508.
- [29] G. Larramona, S. Bourdais, A. Jacob, C. Chone, T. Muto, Y. Cuccaro, B. Delatouche, C. Moisan, D. Pere, G. Dennler, Efficient $\text{Cu}_2\text{ZnSnS}_4$ solar cells spray coated from a hydro-alcoholic colloid synthesized by instantaneous reaction, *RSC Adv.* 4 (2014) 14655–14662.